PAPER

Check for updates

Polydopamine-doped virus-like structured nanoparticles for photoacoustic imaging guided synergistic chemo-/photothermal therapy†

Rong Zhong,[ab] Ruoping Wang,[ab] Xuemei Hou,[ab] Liang Song[*ab] and Yun Zhang [ID] [*abc]

The therapeutic diagnosis effect of cancer commonly depends on the cellular uptake efficiency of nanomaterials. However, the morphology of nanomaterials significantly affects cellular uptake capability. Herein, we designed a polydopamine-doped virus-like structured nanoparticle (GNR@HPMO@PVMSN) composed of a gold nanorod (GNR) core, hollow periodic mesoporous organosilica (HPMO) shell and polydopamine-doped virus-like mesoporous silica nanoparticle (PVMSN) outer shell. Compared with conventional gold nanorod@hollow periodic mesoporous organosilica core−shell nanoparticles (GNR@HPMO), GNR@HPMO@PVMSN with its virus-like structure was proved to enhance the efficiency of cellular uptake. GNR@HPMO@PVMSN with the virtues of high photothermal conversion efficiency and good photoacoustic imaging (PAI) ability was expected to be a promising nanotheranostic agent for imaging guided cancer treatment. The experiments *in vitro* and *in vivo* proved that GNR@HPMO@PVMSN had good biocompatibility as well as photothermal conversion ability. In addition, DOX loading and pH-/NIR-response DOX release abilities of GNR@HPMO@PVMSN were also verified *in vitro*. Therefore, the GNR@HPMO@PVMSN offers a promising strategy for PAI directed synergistic chemo-/photothermal therapy, which improves the therapeutic effect of the nanomaterial on tumors. This work explores the effects of rough surfaces on cellular uptake and provides a versatile theranostic platform for biomedical applications.

Introduction

Recently, nanosystems have been proposed as promising carriers for drugs in cancer treatment owing to their enhanced permeability and retention effect, increasing delivery efficiency and reducing side-effects.[1–10] Mesoporous silica nanoparticles characterized by uniform and tunable mesopores and pore volume and large surface area, as well as easily functionalized surfaces, have stimulated remarkable research interest in biomedicine.[11–14] Much effort has been made to develop sophisticated mesoporous nanoparticles to enhance cellular uptake performance. However, the morphology of nanoparticles has been recognized as a prime important factor influencing intracellular delivery efficiency and cellular uptake process. The rational design of exquisite nanoparticles for effective delivery of theranostic agents to tumors shows great promise for improving treatment efficacy. It is reported that nanoparticles with rough surface properties can enhance adhesion to promote cellular internalization.[4,7,15–18] For example, Xinyan Chen *et al.* constructed rattle-structured nanocapsules (Au@HSN–PGEA, AHPs) with rough surface features, showing a high cellular uptake efficiency.[15] Besides, uniform virus-like mesoporous silica nanoparticles were designed by Wenxing Wang *et al.*, which revealed greatly superior cellular uptake property, unique internalization pathways, and extended blood circulation duration.[16] The presence of rough surface featured with virus-like shapes, is beneficial for the enhanced retention effect as well as cellular uptake performance. Despite that continuous efforts have been devoted to adjusting virus-like shapes of nanoparticles, the complex viral-made procedures are very tedious and it still needs to provide a facile strategy to construct virus-like platforms for tumor therapy.

Polydopamine (PDA) has attracted a great deal of attention, which exhibit broad prospects in various biological field with the virtues of easy preparation method, outstanding biocompatibility, and binding ability with other therapeutic drugs.[19–22] Interestingly, it has been reported that the presence of dopamine could accelerate reaction for preparation of CaCO₃–PDA nanoparticles.[23] Inspired by this phenomenon, we hypothesized that dopamine, with proper measurement, might have great advantages for shorting reaction time as well as improving the

ᵃCAS Key Laboratory of Design and Assembly of Functional Nanostructures, Fujian Provincial Key Laboratory of Nanomaterials, Fujian Institute of Research on the Structure of Matter, Chinese Academy of Sciences, Fuzhou 350002, P. R. China. E-mail: songliang@fjirsm.ac.cn; zhangy@fjirsm.ac.cn

ᵇDepartment of Translational Medicine, Xiamen Institute of Rare-earth Materials, Haixi Institutes, Chinese Academy of Sciences, Xiamen 361021, P. R. China

*ᶜUniversity of Chinese Academy of Sciences, Beijing 100049, P. R. China*

† Electronic supplementary information (ESI) available. See DOI: 10.1039/d0ra02915g

quality of viral silicon. Moreover, polydopamine synthesized by the spontaneous oxidation and polymerization of dopamine under an alkaline solution, possesses strong adhesive properties, which allow almost all of materials to be covered, showing great significance for multifunctional nanoparticles by PDA versatile surface functionalization.[3,24–28] Hence, it is worth highlighting that the introduction of polydopamine may result in a superior therapeutic outcome to fight against tumor.

Gold nanorods, with their peculiar physicochemical properties, are considered as promising agents in diverse biomedical applications including photothermal therapy and photo-acoustic imaging.[29–36] A broad variety of nanosystems toward gold nanorods modification have been developed. Mesoporous silica nanoparticle is an excellent candidate for coating gold nanorods for synergistic chemo-/phototherapy with critical advantages including favorable biocompatibility and drug loading capacity.[37–42] For instance, Lu *et al.* prepared gold nanorod embedded hollow periodic mesoporous organosilica nanospheres, which were also proved to possess high drug loading capacity and excellent biocompatibility.[41] Meanwhile, it has been shown that ratio of ethanol to water played an important role for regulating size of the as-prepared nanoparticles.[43] Among all reports, multiple synthetic strategies were employed to fabricate $Au–SiO_2$ heteronanoparticles with different shapes. However, virus-like structured $Au–SiO_2$ heteronanoparticles are rarely reported. Furthermore, this type of heteronanoparticles could improve intracellular delivery efficiency and cellular uptake process. Based on this point, it is necessary to develop a novel structured $Au–SiO_2$ heteronanoparticles with higher cellular uptake efficiency for tumor therapy.

In our work, we designed a polydopamine-doped virus-like structured nanoparticle (GNR@HPMO@PVMSN) for photo-acoustic imaging (PAI) guided synergistic chemo-/photothermal therapy, which is composed of gold nanorod (GNR) core, hollow periodic mesoporous organosilica (HPMO) shell and polydopamine-doped virus-like mesoporous silica nanoparticle (PVMSN) outer shell (Scheme 1). The absorption peak position and the size of GNR were adjusted by coated with HPMO. Then, GNR@HPMO was covered with PVMSN and the doping of dopamine accelerated the growth of the virus-like structure.
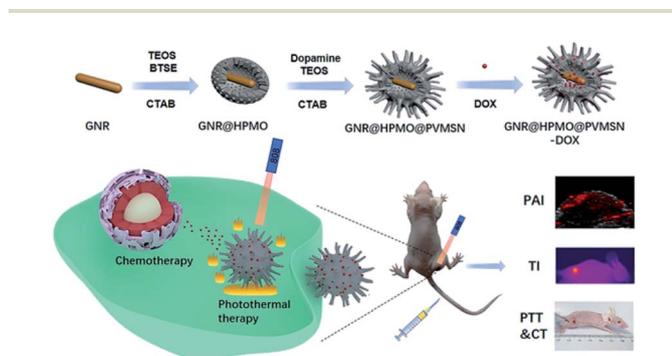
More importantly, the as-prepared GNR@HPMO@PVMSN with the virus-like structure could promote cellular uptake capacity. The experiments *in vitro* and *in vivo* verified that GNR@HPMO@PVMSN had good biocompatibility and photothermal conversion ability. Meanwhile, the loading and pH-/NIR-response release of DOX combined with good photothermal performance and PAI capability improved the therapeutic effect on the tumor.

Experimental

Materials

Hydrogen tetrachloroaurate trihydrate ($HAuCl_4 \cdot 3H_2O$), hexadecyl trimethyl ammonium bromide (CTAB, 99%), sodium borohydride ($NaBH_4$, 99%), doxorubicin (DOX) and tetraethyl orthosilicate (TEOS, 99%) were purchased from Sigma. Sodium oleate (NaOL, CP), silver nitrate ($AgNO_3$, AR), hydrochloric acid (HCl, AR), L-ascorbic acid (AA, 99.99%) were attained from Xilong scientific. Cyclohexane, dopamine hydrochloride (DA·HCl, 98%), H_2O_2 (AR, 30%), ammonia solution ($NH_3 \cdot H_2O$, 25–28%), 1,2-bis(triethoxysilyl)ethane (BTSE, 96%), tri(hydroxymethyl) amino methane hydrochloride (99%) and methanol were purchased from Aladdin Industrial Inc. Sodium hydroxide (NaOH, AR), acetone and nitric acid (AR, 65.0–68.0%) were purchased from Sinopharm Chemical Reagent. DMEM/HIGH glucose and penicillin–streptomycin solutions were purchased from HyClone. Phosphate buffered saline (PBS, 10×) was purchased from Solarbio. Fetal bovine serum (FBS) was purchased from Excell Bio. Cell Counting Kit-8 (CCK-8) and 4′,6-diamidino-2-phenylindole (DAPI) were purchased from Dojindo Laboratories (Japan). The ultrapure water with a resistivity of 18.2 MΩ cm was obtained from Milli-Q Gradient System (Millipore, Bedford, MA, USA) and used for all of the experiments.

Characterization

Transmission electron microscopy (TEM) images were performed on a HITACH H-7650 microscope. Field emission scanning electron microscopy (FE-SEM) images were taken on a Hitachi S-4800 microscope. The UV-VIS-NIR spectra were recorded using a Cary 5000 UV-VIS-NIR spectrophotometer. Inductive coupling plasma Optical emission spectrograph (ICP-OES) was used for Au element amount measurement. The nitrogen adsorption–desorption isotherms and pore size distribution curves were performed at 77 K with a Quantachrome Autosorb iQ2 gas adsorption analyzer. The photothermal performance was examined when it was irradiating the GNR@HPMO@PVMSN solution by 808 nm laser (BTW: diode laser system) and the temperature was recorded by a thermocouple microprobe (STPC-510P, Xiamen Baidewo Technology Co., China). DLS diameter and zeta potential were evaluated on a zeta potential analyzer (Brookhaven Omni, USA).

Synthesis of gold nanorods (GNRs)

Gold nanorods were synthesized according to previous report.[44] Briefly, it contained two steps, first, the synthesis of gold seeds, 250 μL of 10 mM $HAuCl_4$ and 9.75 mL of 0.1 M CTAB aqueous

Scheme 1 Schematic illustration of the design and synthesis of core/shell/shell nanotheranostic GNR@HPMO@PVMSN for PAI guided synergetic chemo-/photothermal therapy.

solution were mixed under magnetic stirring for 10 min. Then, 0.6 mL of cold freshly prepared 10 mM NaBH$_4$ was quickly added with 2 min of vigorous stirring, and stood at 28 °C for 30 min. The colour of the solution changed from yellow to brownish yellow, indicating the formation of gold seeds. Second, the growth of gold nanorods mediated by gold seeds. 7.2 g of CTAB and 0.987 g of NaOL were dissolved in 400 mL of deionized water. Then, 20 mL of 10 mM HAuCl$_4$ was added with gently stirring for 15 min. The colour of the solution changed from yellow to colorless. Next, 8 mL of 10 mM AgNO$_3$ was added and kept stirring for another 5 min. After that, 1.2 mL of HCl was added and stirred for 5 min. Then, 640 μL of 0.1 M AA was added and stirred for 30 s. Next, the prepared 1 mL seed solution was added with vigorous stirring for 30 s. Finally, the above system was kept at 30 °C for 12 h. The resulting solution was centrifuged multiple times and finally dispersed in 20 mL of deionized water for further use.

Synthesis of GNR@HPMO

The synthesis of GNR@HPMO was guided primarily a CTAB mediated sol–gel process and hydrothermal reaction. In brief, 0.12 g of CTAB was dissolved in a mixed solution containing 5.6 mL of ethanol and 10.6 mL of water. Then, 3 mL of the gold nanorod prepared above was added under magnetic stirring, sonicated for 10 min and continuously stirred at 35 °C for 1 h. Next, 0.19 mL of NH$_3$·H$_2$O and a mixture of silane precursors (46.8 μL of TEOS and 46.8 μL of BTSE) were added under vigorous stirring and stirring was continued at 35 °C for 24 h. The resulting product was centrifuged at 10 000 rpm for 5 min and washed with ethanol three times. After that, the obtained product was dispersed in 24 mL of water and stirred at 70 °C for 8 h. Next, the obtained product was collected by centrifugation and redispersed in 24 mL of ethanol, and 48 μL of HCl was added under magnetic stirring, and incubated at 60 °C for 3 hours to remove CTAB multiple times. Finally, the resulting product was washed with water three times and redispersed in 10 mL of water for further use.

Synthesis of GNR@HPMO@PVMSN

GNR@HPMO@PVMSN was synthesized mainly through CTAB as a template and oil–water biphasic reaction. Typically, 1.5 mL of the above prepared GNR@HPMO and 6 mL of 0.1 g CTAB aqueous solution were mixed for 10 min under magnetic stirring. Then, after ultrasonication for 10 min, 50 μL of NaOH (0.1 M) was added under magnetic stirring, and stirring was continued at 65 °C for 2 h. Next, the stirring speed was slowed, and 5 μg of DA·HCl and 20 mL of 8% TEOS/cyclohexane solution were added, and stirring was continued at 65 °C for 16 h. The resulting products were collected by centrifugation and washed with water and ethanol three times, respectively. After that, the obtained products were dispersed in 50 mL of acetone, and stirred at 50 °C for 12 hours to remove CTAB. The samples were collected by centrifugation, washed with ethanol three times, and dispersed in 5 mL of water for further use.

In vitro photothermal performance of GNR@HPMO@PVMSN

To evaluate the photothermal performance, 1 mL sample was added to a quartz cuvette, the distance between the fixed light source and the quartz cuvette were 1 cm and illuminated with an 808 nm laser. First, in order to calculate the photothermal conversion efficiency of the GNR@HPMO@PVMSN, 1 mL of GNR@HPMO@PVMSN solution and 1 mL of aqueous solution were respectively irradiated with an 808 nm laser (2.4 W cm^{-2}) until the temperature was stable. Then turning off the laser, the solution was naturally cooled. Photothermal conversion efficiency could be calculated according to the formula reported by Roper group.[45] In order to evaluate the effect of solution concentration or laser power density on photothermal performance, GNR@HPMO@PVMSN solutions with different concentrations (25, 50, 100, 200, 400 μg mL^{-1}) were irradiated with an 808 nm laser (1.6 W cm^{-2}) for 5 min and equal concentration of GNR@HPMO@PVMSN solutions were irradiated for 5 min under different laser power densities (0.8, 1.6 and 2.4 W cm^{-2}). Finally, we further evaluated the photothermal stability. The GNR@HPMO@PVMSN solution was irradiated with an 808 nm laser (1.6 W cm^{-2}) until the temperature reached 50 °C. Then turning off the laser, the temperature was naturally lowered to 30 °C. The cycle was repeated four times.

DOX loading and controlled releasing

DOX was loaded by GNR@HPMO@PVMSN as follows: 3 mL of 1 mg mL^{-1} DOX methanol solution was mixed with 3 mL of 1 mg mL^{-1} GNR@HPMO@PVMSN in tris buffer solution (pH 8.5). After being stirred at 37 °C for 24 h in the dark, GNR@HPMO@PVMSN–DOX was collected by centrifugation and washed with tris buffer solution (pH 8.5) three times. All washed supernatants were collected for measuring the loading efficiency of DOX using the UV-VIS-NIR spectrophotometer (Agilent Cary 5000) at 480 nm. To study DOX release, 3 mg GNR@HPMO@PVMSN–DOX was dispersed in 5 mL of different PBS buffer solutions (pH 7.4 and pH 5) and packaged in a dialysis bag (molecular weight cut off = 3500 Da). The dialysis bags were placed in 20 mL of each buffer solution and stirred at 37 °C for 48 h. The DOX released in the buffer was collected at the selected time (0.5, 1, 3, 6, 12, 24, 48 h) and measured using the UV-VIS-NIR spectrophotometer at 480 nm. For near-infrared light controllable DOX release experiments, samples in different buffers were exposed to 808 nm laser (2.4 W cm^{-2}) for 5 min after the selected time. The DOX released in the buffer, and after the irradiation, supernatants were collected and measured using the UV-VIS-NIR spectrophotometer at 480 nm. The cumulative released amount of DOX was quantified by the similar method.

Cytotoxicity assay

Hepatoma cell line 7721 cells were cultured in Dulbecco's Modified Eagle's Medium (DMEM) containing 10% FBS and 1% penicillin/streptomycin at 37 °C under 5% CO$_2$. 7721 Cells were incubated in 96-well plates at a density of 1×10^4 cells per well for 24 h. After that, three concentrations of GNR@HPMO@PVMSN (50, 100, and 150 μg mL^{-1}) were added to incubate at 37 °C for 24 h. Next, 10 μL of Cell Counting Kit-8 (CCK-8) was added into each well and incubated for 4 h. The absorbance value was measured using a multi-reader (TECAN,

Infinite M200, Germany) at 450 nm and the viability of cell growth was calculated according to the following formula:

$$\text{Viability (\%)} = (\text{mean absorbance value of treatment group/mean absorbance value of control group}) \times 100\%$$

In vitro chemotherapy and photothermal therapy

7721 cells were incubated in 96-well plates at a density of 1×10^4 cells per well at 37 °C for 24 h. Then, different concentrations of free DOX, GNR@HPMO@PVMSN and GNR@HPMO@PVMSN–DOX were added into each well, respectively. After 6 h of incubation, washed with PBS three times. After that, it was irradiated with 808 nm near-infrared laser (1.6 W cm^{-2}) for 3 min. After incubated for 24 h, cell viability was calculated using CCK-8 assay.

Analysis of cellular uptake

7721 cells were incubated in 24-well plates at a density of 5×10^4 cells per well at 37 °C under 5% CO_2 for 24 h. Two different morphologies of silica nanoparticles and DOX were added into each well. After incubated for different time (5, 15, 30 min, 1, 2 h), the cells were washed with PBS three times. Next, the nucleus was stained with DAPI and the cell fluorescence images were taken with a confocal laser scanning microscope (CLSM). The blue fluorescence of DAPI was excited with a 405 nm laser with an emission channel set at 425–475 nm. The red fluorescence of DOX was excited with a 488 nm laser with an emission channel set at 550–650 nm.

In order to further assess cellular uptake capability, the content of Au in cells was measured. 7721 cells were incubated in 12-well plates at a density of 1×10^5 cells per well for 24 h. Two different morphologies of silica nanoparticles and DOX were added into each well. After incubated for 5, 15, 30 min, 1, 2 h, respectively, the cells were washed with PBS and digested in HNO$_3$. Finally, lysate of the cells was collected and the content of Au was measured by ICP-OES. All experiments were repeated three times.

In vivo biodistribution

For verifying cellular uptake capability in vivo, female BALB/c nude mice (weight 18–22 g) was used as an animal model, which were purchased from Shanghai SLAC Laboratory Animal Co., Ltd. All animal procedures were performed in accordance with the Guidelines for Care and Use of Laboratory Animals of Xiamen University and approved by the Animal Ethics Committee of Xiamen University. Tumor-bearing mice were prepared by Implanting H22 tumor pieces ($3 \times 3 \times 3$ mm^3 in size) into the right hind leg of the nude mice. The animal experiment was performed when the tumor reached approximately 200 mm^3. The Au content (2 mg kg^{-1} of body weight) of GNR@HPMO and GNR@HPMO@PVMSN treatment group was injected into the H22 tumor-bearing mice. After intravenous injection for different time (8, 12 and 24 h), mice were sacrificed to dissect their tumors and the main organs, including heart, liver, spleen, lung, kidney. These tumors and organs were digested in HNO$_3$ for at least 24 h and the Au content in each tissue was measured by ICP-OES.

Photoacoustic imaging (PAI) measurement of GNR@HPMO@PVMSN

For PAI in vitro, GNR@HPMO@PVMSN with different concentrations was placed in a centrifuge tube, and PAI images and the PA intensity were recorded by photoacoustic imaging system (Vevo LAZR-x). For PAI in vivo, tumor-bearing mice with the tumor size of about 200 mm^3 were treated with 100 μL of GNR@HPMO@PVMSN (1 mg mL^{-1}) through intravenous injection. After intravenous injection for 24 h, the PAI images and the PA intensity of the tumor sites of the mice were recorded by photoacoustic imaging system (Vevo LAZR-x).

In vivo infrared thermal imaging (TI) measurement of GNR@HPMO@PVMSN

Tumor-bearing mice with the tumor size of about 200 mm^3 were treated with PBS or GNR@HPMO@PVMSN through intravenous injection. After intravenous injection for 24 h, the tumor site was irradiated with an 808 nm laser (1.5 W cm^{-2}) for 5 min. Temperature changed and near-infrared heating images were recorded by infrared thermal camera (Fotric 225).

In vivo chemotherapy and photothermal therapy

When the tumor grew to a size of about 200 mm^3, the tumor-bearing mice were divided into 6 groups ($n = 5$). Control group: mice were treated with PBS through intravenous injection. Test group: mice were treated with PBS + NIR, GNR@HPMO@PVMSN, GNR@HPMO@PVMSN + NIR, GNR@HPMO@PVMSN–DOX, GNR@HPMO@PVMSN–DOX + NIR. For all NIR irradiation groups, all tumors were completely covered with laser irradiation (808 nm, 2.0 W cm^{-2}) for 5 min after intravenous injection for 24 h. Body weight and tumor size were recorded every other day until the 16th day. Mice were euthanized and representative tumors were weighed and imaged. Finally, histological detection was carried out. The main organs including heart, liver, spleen, lung, kidney and tumor of tumor-bearing mice were collected and each sample was stained with hematoxylin and eosin (H&E).

Statistical methods

All experiments were performed at least three times except as specified. Experimental data was expressed as mean ± standard deviation. Statistical analysis was performed by one-way ANOVA for SPSS 17.0. *$P < 0.05$ was considered statistically significant and **$P < 0.01$ was considered statistically extreme significant.

Results and discussion

Synthesis and characterization of GNR@HPMO@PVMSN

The synthetic procedure of GNR@HPMO@PVMSN is illustrated in Scheme 1. First, the GNRs were synthesized using the seed growth method. Transmission electron microscopy (TEM) image (Fig. 1a) shows that the synthesized GNRs have a uniform
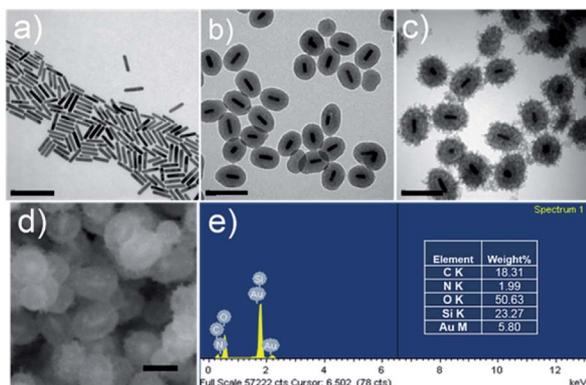
Fig. 1 TEM images of (a) GNR, (b) GNR@HPMO, and (c) GNR@HPMO@PVMSN. Scale bar, 200 nm; (d) SEM image of GNR@HPMO@PVMSN, scale bar, 100 nm; (e) the elemental analysis of GNR@HPMO@PVMSN.

size of about 77.24 ± 7.64 nm in length and 17.34 ± 1.17 nm in width. Dynamic light scattering (DLS) analysis (Fig. S1a and Table S1†) reveals that the average size of the GNRs is about 63.24 nm. GNRs were coated with HPMO by a hydrothermal method using hexadecyl trimethyl ammonium bromide (CTAB) as a template, tetraethoxysilane (TEOS) and 1,2-bis(triethoxysilyl)ethane (BTSE) as precursors. TEM image (Fig. 1b) shows that GNR@HPMO was successfully synthesized, the thickness of HPMO shells is 36.55 ± 2.52 nm, and the length and width of these GNRs decreased to 58.55 ± 5.86 nm and 16.44 ± 1.58 nm, respectively. As shown in DLS result (Fig. S1b and Table S1†), the average diameter of GNR@HPMO is about 127.14 nm. Moreover, the size of the GNR@HPMO can be tuned from ∼120 to ∼200 nm by changing the ratio of ethanol/water from 0.30 to 0.39 (Fig. 1b and S2†). Finally, the obtained GNR@HPMO was coated with PVMSN through oil–water biphase microemulsion method according to the synthetic method of Au@virus-like mesoporous silica with a slight modification.[16] In this biphase system, the upper oil phase was a TEOS/cyclohexane solution, while the bottom water phase was an aqueous solution of CTAB as a template, NaOH as a catalyst, dopamine hydrochloride (DA·HCl) and GNR@HPMO. TEM (Fig. 1c) reveals that GNR@HPMO was successfully coated with PVMSN and the thickness of PVMSN shells increased to 63.56 ± 4.75 nm. As shown in DLS result (Fig. S1c and Table S1†), the average diameter of GNR@HPMO@PVMSN is about 201.27 nm.

To further demonstrate the successful preparation of GNR@HPMO@PVMSN, a series of characterization analysis were implemented as follows. The nitrogen adsorption results (Fig. S3a and c†) show that the adsorption–desorption isotherms of GNR@HPMO and GNR@HPMO@PVMSN are a type IV curve of the mesoporous structure. The BET surface area, total pore volume, and average pore diameter of GNR@HPMO are 703.145 m^2 g^{-1}, 1.219 cm^3 g^{-1}, and 6.93 nm, respectively (Fig. S3a and b†). In contrast, the specific surface area and total pore volume of GNR@HPMO@PVMSN decreased to 145.54 m^2 g^{-1} and 0.5165 cm^3 g^{-1}, respectively, and the average pore size increased to 14.20 nm (Fig. S3c and d†), which

could be attributed to the function of silica branches. In the virus-like structure, mesoporous silica branches are arranged intricately with each other, resulting in an increase of average pore diameter. Meanwhile, with the pore diameter of polydopamine-doped virus-like mesoporous silica decreasing, the specific surface area and total pore volume of GNR@HPMO@PVMSN decreased. More importantly than this phenomenon, the doping of dopamine could promote the formation of the virus-like structure compared with the reaction without dopamine (Fig. S4†). In addition, a field emission scanning electron microscopy (FE-SEM) images (Fig. 1d) and energy dispersive spectrometer (EDS) elemental analysis (Fig. 1e) also demonstrate that GNR@HPMO@PVMSN has been successfully synthesized, which has a core–shell–shell structure and contains C, O, Si and a small amount of Au, N elements.

Photothermal performance of GNR@HPMO@PVMSN

We further verified the near-infrared absorption performance of the as-prepared GNR@HPMO@PVMSN. As shown in Fig. 2a, a strong absorption peak position of GNR is around 917 nm. Then, the absorption peak position occurred a blue-shift changing to 787 nm after coated with HPMO, which was caused by the change of GNR in size. Thereafter, GNR@HPMO was coated with PVMSN and the absorption peak is slightly red-shifted to around 808 nm, which was in the NIR range, showing important significance for photothermal property. These above results suggest that the absorption peak of the synthetic GNR@HPMO@PVMSN can be adjusted by changing the reaction conditions of GNR, GNR@HPMO, or GNR@HPMO@PVMSN to reach an ideal state. Next, in order to investigate the photothermal performance of the GNR@HPMO@PVMSN, the temperature rise and fall curve of GNR@HPMO@PVMSNs aqueous solution were measured. Photothermal conversion efficiency was calculated according to the formula reported by Roper group,[45] which was 56.3% (Fig. 2b and c). Then, we measured the heating curves of GNR@HPMO@PVMSN with different concentrations at the same time under the same laser power density, the heating curves of different laser power densities at the same
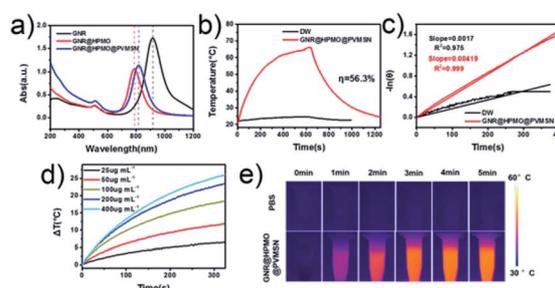

Fig. 2 (a) UV-VIS-NIR absorption spectra of GNR, GNR@HPMO, and GNR@HPMO@PVMSN; (b and c) photothermal conversion efficiency of GNR@HPMO@PVMSN aqueous solution (200 μg mL^{-1}) under 808 nm laser irradiation (2.4 W cm^{-2}); (d) temperature curves of different concentrations of GNR@HPMO@PVMSN aqueous solution; (e) infrared thermal images of PBS, GNR@HPMO@PVMSN aqueous solution under continuous NIR laser irradiation (1.6 W cm^{-2}) for 5 min.

concentration for the same time, and the temperature rise and fall curves for four cycles. These results (Fig. 2d, S5a and b†) show that the GNR@HPMO@PVMSN is a concentration-dependent and power-dependent photothermal material with good photothermal stability. Finally, the infrared thermal images (Fig. 2e) show that compared with the PBS solution, the temperature of GNR@HPMO@PVMSN aqueous solution could reach 50 °C after irradiation for 5 min, which is sufficient to kill the tumor cells. Therefore, high photothermal conversion efficiency and good photothermal stability determine GNR@HPMO@PVMSN as a potential photothermal therapy reagent.

pH-/NIR-responsive drug release

A successful fabrication of DOX-loaded virus-like structured nanoparticles was confirmed. We immediately turned to evaluate the properties of GNR@HPMO@PVMSN for encapsulation and controlled release of DOX. As shown in Fig. S6,† GNR@HPMO@PVMSN was incubated in PBS solution at pH 7.4 and 5.0 for 3 and 6 days respectively. Compared with the TEM image at day 0, the morphology of GNR@HPMO@PVMSN did not change significantly, indicating that GNR@HPMO@PVMSN was stable in different pH values. UV-VIS-NIR absorption spectrum (Fig. S7a†) shows GNR@HPMO@PVMSN–DOX emerges a characteristic peak of DOX located at the wavelengths of 233 nm and 253 nm. Besides, the zeta potential (Fig. S7b†) of GNR@HPMO@PVMSN–DOX changes from the original -15 ± 3.2 mV to -7 ± 2.5 mV. The above results indicate the well prepared of GNR@HPMO@PVMSN–DOX. The DOX loading efficiency was calculated about $21.8 \pm 1.6\%$ by UV calibration curves of DOX. It is pointed that mesoporous structure and interior space of the GNR@HPMO@PVMSN and the interaction force such as π–π bonds, hydrogen bonds and electrostatic incorporation between the doping of polydopamine and DOX are the benefit for loading drug. Next, we explored the *in vitro* cumulative drug release profiles at different pH values under with/without laser. The *in vitro* release profiles showed the DOX released at pH 5.0 faster than at pH 7.4 (Fig. 3a), which may be attributed to the protonation of the amino group of polydopamine and/or the DOX molecules under acidic condition. Moreover, the release of DOX increased from GNR@HPMO@PVMSN–DOX at pH 5.0 under 808 nm NIR laser (2.4 W cm^{-2}) for 5 min. While no significant change was observed at pH 7.0 under the same conditions (Fig. 3b). Consequently, we fully believe that GNR@HPMO@PVMSN–DOX with a pH-/NIR-response drug release property can be used as a promising applicable nanocarriers for drug delivery.

In vitro cytotoxicity assay and antitumor effect

GNR@HPMO@PVMSN with good photothermal performance and controllable drug release capacity could be used as a promising nanoplatform for synergistic chemo-/photothermal therapy. Therefore, we further evaluated the cytotoxicity of GNR@HPMO@PVMSN using CCK-8 kit assay *in vitro*. As shown in Fig. 4d, the cell viability of Hepatoma cells (7721) incubated with different concentrations of GNR@HPMO@PVMSN
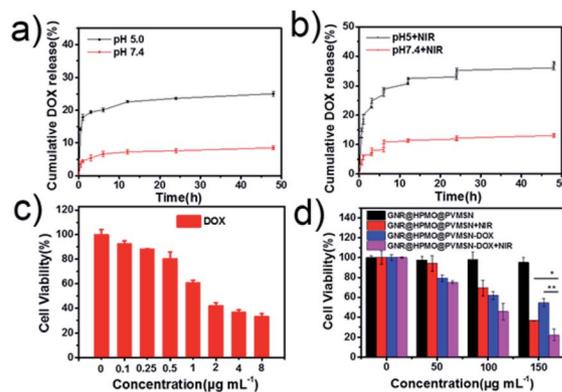

Fig. 3 (a) DOX release from GNR@HPMO@PVMSN–DOX at pH 7.4 and 5.0 at 37 °C, and (b) NIR-triggered release of DOX from GNR@HPMO@PVMSN–DOX at pH 7.4 and 5.0, which were irradiated with an 808 nm NIR laser (1.6 W cm^{-2}) for 5 min at different time points; (c and d) cell viability of 7721 cells treated by DOX with different concentrations, and treated by GNR@HPMO@PVMSN and GNR@HPMO@PVMSN–DOX with or without 808 nm NIR irradiation (1.25 W cm^{-2}) for 3 min.

ranging from 0 to 200 mg mL^{-1} for 24 h are still higher than 90% *in vitro*. This result suggests GNR@HPMO@PVMSN has good biocompatibility. To demonstrate the synergistic therapeutic effect *in vitro*, 7721 cells were treated with DOX, GNR@HPMO@PVMSN + NIR, GNR@HPMO@PVMSN–DOX, GNR@HPMO@PVMSN–DOX + NIR, respectively. The results (Fig. 4c and d) show that as the concentration of DOX increased, the viability of 7721 cells decreased continuously. Furthermore, the cell viability of the GNR@HPMO@PVMSN + NIR, GNR@HPMO@PVMSN–DOX, GNR@HPMO@PVMSN–DOX + NIR treatment groups decreased with the increase of the concentration of material, and the cell viability could reach 20%. The above results indicate that GNR@HPMO@PVMSN has a good synergistic chemo-/photothermal therapy ability of tumor cells *in vitro*.

Analysis of cellular uptake

To further confirm higher cellular uptake mediated by GNR@HPMO@PVMSN, 7721 cells were treated with DOX, GNR@HPMO, GNR@HPMO@PVMSN, keeping the same
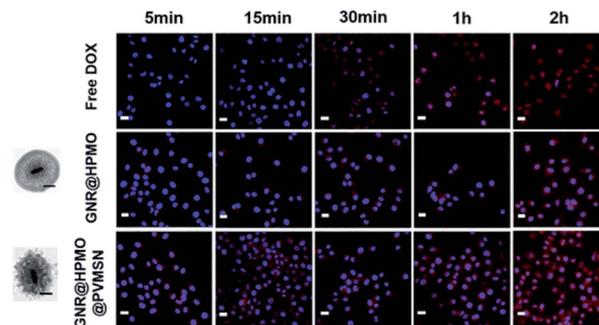

Fig. 4 CLSM images of the 7721 cells incubated with DOX, GNR@HPMO, and GNR@HPMO@PVMSN (scale bar, 50 nm) for 5, 15, 30 min, 1 and 2 h. Scale bar, 20 μm.

particle size between GNR@HPMO and GNR@HPMO@PVMSN. 7721 cells were washed with PBS solution after incubated for 5, 15, 30 min, 1, 2 h, respectively, measured by confocal laser scanning microscope (CLSM). GNR@HPMO@PVMSN group showed obviously superior cellular uptake efficiency to the other two groups (Fig. 4). To further confirm the cellular uptake abilities *via* quantification analysis, we analyzed the content of Au in 7721 cells. GNR@HPMO@PVMSN treatment group presented higher uptake level compared with GNR@HPMO groups (Fig. S8†). In addition, we further explored cellular uptake rate of GNR@HPMO and GNR@HPMO@PVMSN after cultured with cells for 24 h by using DAPI as nuclear staining reagent and FITC as fluorescent labeling of materials. As shown in Fig. S9,† the GNR@HPMO@PVMSN group had a higher cellular uptake efficiency than the GNR@HPMO group after cultured with cells for 24 h. Owing to the rough surface composed of spike, virus can bind strongly to cell membranes during the rapid invasion process.[16,46] Many nanoparticles mimicking viruses with rough surface consisting of spike has been demonstrated to have good cellular invasion properties.[4,7] Thus, it can be indicated that virus-like structure made a great significance in the enhancement of cellular uptake efficiency.

In vivo biodistribution

For monitoring the distribution of as-prepared GNR@HPMO@PVMSN *in vivo*, we measured the content of Au in the heart, liver, spleen, lung, kidney and tumors of H22 tumor-bearing mice using ICP-OES at different time (8, 12 and 24 h) of post-injection, respectively. As can be seen from the Fig. 5a, GNR@HPMO@PVMSN is mainly distributed in the liver, spleen and lung, and as time increased, the GNR@HPMO@PVMSN continuously increased in the tumor site. We also explored the tumor uptake capacity of GNR@HPMO and GNR@HPMO@PVMSN *in vivo*. It can be seen that GNR@HPMO@PVMSN had more aggregation in the tumor site than GNR@HPMO at different time (Fig. 5b). This result further suggests that the virus-like structure of the material is beneficial to promote tumor uptake *in vivo*.

Photoacoustic imaging (PAI) and infrared thermal imaging (TI) measurement

In order to evaluate the PAI ability of GNR@HPMO@PVMSN, we conducted a photoacoustic signal exploration of GNR@HPMO@PVMSN from *in vitro* to *in vivo* using the

photoacoustic imaging system (Vevo LAZR-x). The result (Fig. 6a) shows that the intensity of PA signal improved gradually as the concentration of GNR@HPMO@PVMSN increased. For evaluating PAI *in vivo*, we intravenously injected GNR@HPMO@PVMSN and GNR@HPMO into a tumor-bearing mouse. As shown in Fig. 6b, compared with GNR@HPMO, the PA signal of GNR@HPMO@PVMSN was more significantly enhanced after 24 h of post-injection, confirming more sufficient accumulation of GNR@HPMO@PVMSN in the tumor site, keeping consistent with the result by semi-quantitative analysis (Fig. S10a†). These results further demonstrate the polydopamine-doped virus-like structure can enhance the uptake capacity of tumor cells and increase the accumulation in tumor. In addition, we further assessed photothermal properties *in vivo*. The tumor-bearing mice was irradiated under 808 nm laser (0.8 W cm^{-2}, 5 min) after intravenous injection of GNR@HPMO@PVMSN for 24 h. It is found that the temperature of GNR@HPMO@PVMSN increased rapidly to 50 °C after 5 min of irradiation, while PBS group rose slightly and only reached the highest temperature of 41.9 °C (Fig. 6c and S10b†), confirming the possibility of GNR@HPMO@PVMSN as photothermal agents for PTT *in vivo*.

In vivo chemotherapy and photothermal therapy

Encouraged by the good PAI and photothermal properties of the GNR@HPMO@PVMSN, we further evaluated the synergistic chemo-/photothermal therapy efficacy of the GNR@HPMO@PVMSN *in vivo*. Tumor-bearing mice were randomly divided into 6 groups ($n = 5$) and treated with PBS, PBS + NIR, GNR@HPMO@PVMSN, GNR@HPMO@PVMSN + NIR, GNR@HPMO@PVMSN–DOX, GNR@HPMO@PVMSN–DOX + NIR, respectively. The tumor size and body weight of the mice were measured every other day until the 16th day. After treatment, the tumor was taken out from the different groups of mice and weighed. The result (Fig. 7a) shows that there was no significant change in body weight of each group
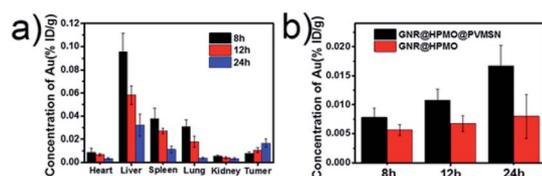

Fig. 5 (a) Time-dependent biodistribution of GNR@HPMO@PVMSN *in vivo*; (b) the Au content in tumor after intravenous injection with GNR@HPMO, and GNR@HPMO@PVMSN for different time (8, 12 and 24 h).
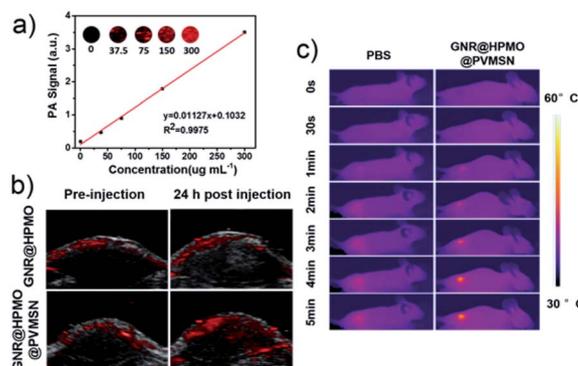

Fig. 6 (a) PA intensity and corresponding PA images of GNR@HPMO@PVMSN solution of different concentrations; (b) PA images of the tumor-bearing mice before and after intravenous injection with GNR@HPMO@PVMSN and GNR@HPMO for 24 h; (c) infrared thermal images of tumor-bearing mice after intravenous injection with PBS or GNR@HPMO@PVMSN for 24 h exposed to the 808 nm laser (0.8 W cm^{-2}) for 5 min.
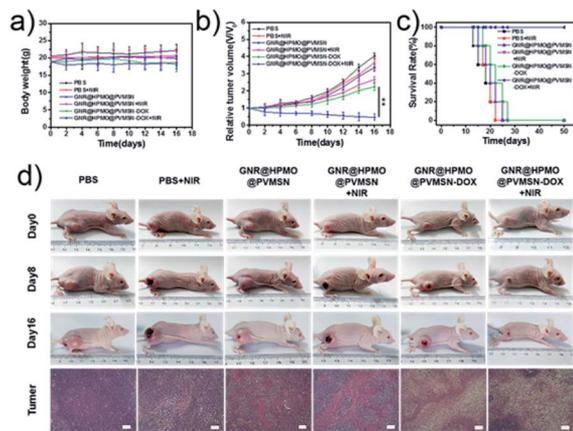
Fig. 7 (a) Body weight, (b) relative tumor volume and (c) the survival rate of the mice after treatment with PBS as control, PBS + NIR, GNR@HPMO@PVMSN, GNR@HPMO@PVMSN + NIR, GNR@HPMO@PVMSN−DOX, and GNR@HPMO@PVMSN−DOX + NIR, respectively; (d) representative images of tumor-bearing mice for varied time periods and representative H&E stained images of tumors after 16 day of therapy in different treatment groups. Scale bar, 200 μm.

of mice, indicating that the material has good biocompatibility in the system and no obvious toxicity. The results (Fig. 7b and S11†) show that there was a significant delay in tumor growth in the GNR@HPMO@PVMSN + NIR and GNR@HPMO@PVMSN−DOX treated group compared with the PBS treated group, proving that photothermal therapy alone or chemotherapy alone had a local inhibitory effect on the tumor. However, the GNR@HPMO@PVMSN−DOX + NIR treatment group had the best therapeutic effect on the tumor where the tumor was basically inhibited. Hematoxylin and eosin (H&E) staining (Fig. 7d) images of the tumor further show that comparing to PBS group, the tumor cells of other groups were subjected to different degrees of damage, apoptosis or necrosis and the efficient killing effect of GNR@HPMO@PVMSN−DOX + NIR treatment group was remarkable. All results indicate that the synergistic antitumor efficiency of PTT and chemotherapy based on GNR@HPMO@PVMSN was especially prominent, and superior to treatment with PTT or chemotherapy alone. In addition, the survival rate was recorded for 50 d after treatment and the survival rate of GNR@HPMO@PVMSN−DOX + NIR treatment group was maintained at 100% (Fig. 7c). The result demonstrated that GNR@HPMO@PVMSN−DOX offers excellent PTT and chemotherapy effect for inhibit tumor growth and extend survival rate. Finally, the safety assessment of other organs was carried out. H&E staining images (Fig. S12†) of heart, liver, spleen, lung, and kidney show that there are no obvious side effects between the organs in each group compared with the PBS treatment group, demonstrating that the GNR@HPMO@PVMSN has negligible systemic toxicity and good biocompatibility. Therefore, the prepared GNR@HPMO@PVMSN has potential applications in the synergistic chemo-/photothermal therapy of tumor *in vivo*.

Conclusions

In summary, a multifunctional polydopamine-doped virus-like structured nanoparticle (GNR@HPMO@PVMSN) for PAI directed synergistic chemo-/photothermal therapy was successfully constructed. GNR@HPMO@PVMSN displays good photothermal conversion efficiency and outstanding PAI capability. This "ship-in-a-bottle" was employed to produce GNR core inside the cavity, virus-like mesoporous silica was employed to preserve the rough surface feature, and the interior space was used for drug loading. Doping of dopamine promotes the growth of virus-like mesoporous silica. Meanwhile, the proposed virus-like structure was proved to enhance the efficiency of cellular uptake. In addition, the loading and controlled release of DOX enable the GNR@HPMO@PVMSN to have the synergistic chemo-/photothermal therapy ability. *In vitro* and *in vivo* results confirm the virus-like structure provided much better therapeutic effect on the tumor. We hope that this work will offer a powerful theranostic reagent for PAI directed synergistic chemo-/photothermal therapy.

Conflicts of interest

There are no conflicts to declare.

Acknowledgements

Notes and references

1 E. Blanco, H. Shen and M. Ferrari, *Nat. Biotechnol.*, 2015, **33**, 941–951.
2 J. Ding, J. Chen, L. Gao, Z. Jiang, Y. Zhang, M. Li, Q. Xiao, S. S. Lee and X. Chen, *Nano Today*, 2019, **29**, 100800–100818.
3 J. Kong, Y. Wang, J. Zhang, W. Qi, R. Su and Z. He, *Angew. Chem., Int. Ed.*, 2018, **57**, 14032–14036.
4 Y. Li, J. Lin, P. Wang, Q. Luo, H. Lin, Y. Zhang, Z. Hou, J. Liu and X. Liu, *ACS Nano*, 2019, **13**, 12912–12928.
5 S. Liu, J. Yang, H. Jia, H. Zhou, J. Chen and T. Guo, *ACS Appl. Mater. Interfaces*, 2018, **10**, 23630–23637.
6 W. L. Liu, T. Liu, M. Z. Zou, W. Y. Yu, C. X. Li, Z. Y. He, M. K. Zhang, M. D. Liu, Z. H. Li, J. Feng and X. Z. Zhang, *Adv. Mater.*, 2018, **30**, 1802006–1802015.
7 Y. Niu, M. Yu, S. B. Hartono, J. Yang, H. Xu, H. Zhang, J. Zhang, J. Zou, A. Dexter, W. Gu and C. Yu, *Adv. Mater.*, 2013, **25**, 6233–6237.
8 K. Yang, Y. Liu, Y. Wang, Q. Ren, H. Guo, J. B. Matson, X. Chen and Z. Nie, *Biomaterials*, 2019, **223**, 119460.
9 C. Dong, Q. Jiang, X. Qian, W. Wu, W. Wang, L. Yu and Y. Chen, *Nanoscale*, 2020, **12**, 5587–5600.
10 C. Zhang, J. Li, C. Yang, S. Gong, H. Jiang, M. Sun and C. Qian, *Nanomedicine*, 2020, **23**, 102071.

11 W. Cheng, J. Nie, N. Gao, G. Liu, W. Tao, X. Xiao, L. Jiang, Z. Liu, X. Zeng and L. Mei, *Adv. Funct. Mater.*, 2017, **27**, 1704135–1704149.

12 S. Jafari, H. Derakhshankhah, L. Alaei, A. Fattahi, B. S. Varnamkhasti and A. A. Saboury, *Biomed. Pharmacother.*, 2019, **109**, 1100–1111.

13 H. Zhang, X. Wang, P. Wang, R. Liu, X. Hou, W. Cao, R. Zhong, X. Liu and Y. Zhang, *RSC Adv.*, 2018, **8**, 37433–37440.

14 M. Zhang, X. Liu, Q. Luo, Q. Wang, L. Zhao, G. Deng, R. Ge, L. Zhang, J. Hu and J. Lu, *Chem. Eng. J.*, 2020, **389**, 124450.

15 X. Chen, Q. Zhang, J. Li, M. Yang, N. Zhao and F. J. Xu, *ACS Nano*, 2018, **12**, 5646–5656.

16 W. Wang, P. Wang, X. Tang, A. A. Elzatahry, S. Wang, D. Al-Dahyan, M. Zhao, C. Yao, C. T. Hung, X. Zhu, T. Zhao, X. Li, F. Zhang and D. Zhao, *ACS Cent. Sci.*, 2017, **3**, 839–846.

17 H. Wu, D. Zhong, Z. Zhang, Y. Li, X. Zhang, Y. Li, Z. Zhang, X. Xu, J. Yang and Z. Gu, *Adv. Mater.*, 2020, 1904958.

18 Z. Zhang, X. Zhang, X. Xu, Y. Li, Y. Li, D. Zhong, Y. He and Z. Gu, *Adv. Funct. Mater.*, 2015, **25**, 5250–5260.

19 H. Li, Y. Jia, H. Peng and J. Li, *Adv. Colloid Interface Sci.*, 2018, **252**, 1–20.

20 C. Qi, L.-H. Fu, H. Xu, T.-F. Wang, J. Lin and P. Huang, *Sci. China: Chem.*, 2019, **62**, 162–188.

21 H. Q. Tran, R. Batul, M. Bhave and A. Yu, *Biotechnol. J.*, 2019, **14**, 1900080–1900091.

22 Z. Wang, Y. Duan and Y. Duan, *J. Controlled Release*, 2018, **290**, 56–74.

23 Z. Dong, L. Feng, Y. Hao, M. Chen, M. Gao, Y. Chao, H. Zhao, W. Zhu, J. Liu, C. Liang, Q. Zhang and Z. Liu, *J. Am. Chem. Soc.*, 2018, **140**, 2165–2178.

24 Y.-W. Chen, Y.-K. Peng, S.-W. Chou, Y.-J. Tseng, P.-C. Wu, S.-K. Wang, Y.-W. Lee, J.-J. Shyue, J.-K. Hsiao, T.-M. Liu and P.-T. Chou, *Part. Part. Syst. Charact.*, 2017, **34**, 1600415–1600426.

25 X. Li, M. Jiang, S. Zeng and H. Liu, *Theranostics*, 2019, **9**, 3866–3878.

26 G. Liu, N. Gao, Y. Zhou, J. Nie, W. Cheng, M. Luo, L. Mei, X. Zeng and W. Deng, *Pharmaceutics*, 2019, **11**, 507–524.

27 R. Mrówczyński, A. Nan, R. Turcu, J. Leistner and J. Liebscher, *Macromol. Chem. Phys.*, 2015, **216**, 211–217.

28 T. Repenko, A. Rix, A. Nedilko, J. Rose, A. Hermann, R. Vinokur, S. Moli, R. Cao-Milàn, M. Mayer, G. von Plessen, A. Fery, L. De Laporte, W. Lederle, D. N. Chigrin

and A. J. C. Kuehne, *Adv. Funct. Mater.*, 2018, **28**, 1705607–1705614.

29 Q. Dong, X. Wang, X. Hu, L. Xiao, L. Zhang, L. Song, M. Xu, Y. Zou, L. Chen, Z. Chen and W. Tan, *Angew. Chem., Int. Ed.*, 2018, **57**, 177–181.

30 B. Jang, J.-Y. Park, C.-H. Tung, I.-H. Kim and Y. Choi, *ACS Nano*, 2011, **5**, 1086–1092.

31 P. M. Lakhani, S. V. Rompicharla, B. Ghosh and S. Biswas, *Nanotechnology*, 2015, **26**, 432001–432016.

32 Y. Huang, Q. Liu, Y. Wang, N. He, R. Zhao, J. Choo and L. Chen, *Nanoscale*, 2019, **11**, 12220–12229.

33 W. Zhang, Y. Wang, X. Sun, W. Wang and L. Chen, *Nanoscale*, 2014, **6**, 14514–14522.

34 Y. Huang, N. He, Y. Wang, D. Shen, Q. Kang, R. Zhao and L. Chen, *J. Mater. Chem. B*, 2019, **7**, 1149–1159.

35 D. Lin, T. Qin, Y. Wang, X. Sun and L. Chen, *ACS Appl. Mater. Interfaces*, 2014, **6**, 1320–1329.

36 C. Liu, L. Zhang, X. Chen, S. Li, Q. Han, L. Li and C. Wang, *Chem. Eng. J.*, 2020, **382**, 122720–122729.

37 S. Fang, J. Lin, C. Li, P. Huang, W. Hou, C. Zhang, J. Liu, S. Huang, Y. Luo, W. Fan, D. Cui, Y. Xu and Z. Li, *Small*, 2017, **13**, 1602580–1602588.

38 A. Garcia-Fernandez, E. Aznar, R. Martinez-Manez and F. Sancenon, *Small*, 2020, **16**, 1902242–1902303.

39 C. Li, Y. Zhang, Z. Li, E. Mei, J. Lin, F. Li, C. Chen, X. Qing, L. Hou, L. Xiong, H. Hao, Y. Yang and P. Huang, *Adv. Mater.*, 2018, **30**, 1706150–1706157.

40 Z. Qi, J. Shi, Z. Zhang, Y. Cao, J. Li and S. Cao, *Mater. Sci. Eng., C*, 2019, **104**, 109889–109899.

41 J. Wu, Y. Liu, Y. Tang, S. Wang, C. Wang, Y. Li, X. Su, J. Tian, Y. Tian, J. Pan, Y. Su, H. Zhu, Z. Teng and G. Lu, *ACS Appl. Mater. Interfaces*, 2016, **8**, 17927–17935.

42 Z. Zhang, L. Wang, J. Wang, X. Jiang, X. Li, Z. Hu, Y. Ji, X. Wu and C. Chen, *Adv. Mater.*, 2012, **24**, 1418–1423.

43 Z. Teng, J. Zhang, W. Li, Y. Zheng, X. Su, Y. Tang, M. Dang, Y. Tian, L. Yuwen, L. Weng, G. Lu and L. Wang, *Small*, 2016, **12**, 3550–3558.

44 S.-R. Wu, X.-D. Tian, S.-Y. Liu, Y. Zhang and J.-F. Li, *J. Raman Spectrosc.*, 2018, **49**, 659–667.

45 D. K. Roper, W. Ahn and M. Hoepfner, *J. Phys. Chem. C*, 2007, **111**, 3636–3641.

46 C. Xu, Y. Niu, A. Popat, S. Jambhrunkar, S. Karmakar and C. Yu, *J. Mater. Chem. B*, 2014, **2**, 253–256.